Discrete Element Modelling of Flexible Membrane Boundaries for Triaxial Tests

Tongming Qu[a], Y.T. Feng[a], Yong Wang[b] and Min Wang[c]

[a]Zienkiewicz Centre for Computational Engineering, College of Engineering, Swansea University, Swansea, Wales SA1 8EP, UK

[b]State Key Laboratory of Geomechanics and Geotechnical Engineering, Institute of Rock and Soil Mechanics, Chinese Academy of Sciences, Wuhan, China

[c]T-3 Fluid Dynamics and Solid Mechanics Group, Theoretical Division, Los Alamos National Laboratory, Los Alamos, New Mexico, 87545, USA

Abstract:

The discrete element modelling (DEM) of triaxial tests plays a critical role in unveiling fundamental properties of particulate materials, but the numerical implementation of a flexible membrane boundary for the testing still imposes problems. In this study, a robust algorithm was proposed to reproduce a flexible membrane boundary in triaxial testing. The equivalence of strain energy enables the particle-scale parameters representing the flexible membrane to be directly determined from the real geometric and material parameters of the membrane. Then the proposed flexible membrane boundary was implemented in the context of discrete element simulation of triaxial testing and was validated with laboratory experiments. Furthermore, comparisons of triaxial tests with flexible and rigid boundaries were performed from macro-scale to meso-scale. The results show that the boundary condition has limited influences on the stress-strain behaviour but a relatively large impact on the volumetric change, the failure mode, the distribution of contact forces, and the fabric evolution of particles in the specimen during triaxial testing.

Keywords: DEM, Triaxial Tests, Flexible Membrane Boundary, Strain Energy, Shear Band, Fabric Evolution

1 Introduction

The triaxial test has long been one of the most fundamental methods for geotechnical testing. It is commonly used to determine the strength and stiffness of soil and rock for engineering design and construction. Furthermore, it also acts as the calibration foundation for theoretical developments, such as the development of constitutive relations for geotechnical materials. The extensive use of triaxial tests in practice and research has encouraged a large body of work to fully understand the mechanical behaviour of the specimen during triaxial testing.

The discrete element method (DEM) is a powerful numerical method for reproducing the behaviour of granular materials and has exhibited particular superiorities over conventional continuum mechanics based methods, such as finite element methods (FEM) and finite difference methods (FDM). Numerical triaxial tests have long been used for meso-scale parameters calibration for geotechnical discrete element models. The details of triaxial cells vary from laboratory to laboratory but the sides of testing samples are almost always covered with a flexible rubber or latex membrane which allows implementation of hydrostatic confining stress. It is the DEM simulation of the latex membrane boundary during triaxial shearing that has suffered from unquantifiable errors.

Existing research has shown that the confining membrane can dramatically affect the behaviour of tested triaxial samples [1, 2]. Henkel and Gilbert [3] found that the measured clay strength bounded by the standard rubber membrane increased by 14% compared with unconfined compressed tests. Vermeer [4] showed that the formation and development of shear band are closely related to membrane properties, particularly for larger-sized particles. Therefore, a critical issue for the accurate DEM modelling of triaxial tests consists in realistically representing the latex/rubber

membrane.

The most straightforward strategy is to assume a rigid wall boundary [5, 6]. By using the servo control mechanism on a rigid wall, external forces will be imposed on the outer layer of particles in the sample and a relatively uniform stress distribution within the specimen can be iteratively obtained. However, this widely used boundary treatment approach is fundamentally different from a flexible membrane boundary: 1) The rigid boundary prohibits the development of strain localization within the specimen during axial loading; 2) the rigid constraint leads to an oversized confining pressure at the local failure zone and may mistakenly estimate a wrong strength of the tested specimen, giving rise to different post-peak behaviours; 3) Particles close to the rigid wall are inclined to align with the boundary, causing some regular particle packing configurations and non-uniform stress distributions along the boundary [7].

In this paper, existing membrane treatment approaches for triaxial tests were first critically reviewed within the DEM framework. Then a physically more realistic ball representation method for flexible membranes was proposed in detail. To verify the method, numerical results for triaxial tests simulated with the proposed flexible membrane were compared with experimental results. In addition, to show the influence of the boundary on the mechanical behaviour of the specimen during triaxial loading, some critical features at both particle-scale and macro-scale in specimens enclosed with rigid and flexible boundaries were investigated.

2 Overview of flexible membrane simulation

To accurately apply the hydrostatic confining stress but at the same time to allow free deformation of the membrane boundary are two main difficulties imposed to the DEM modelling of triaxial tests with latex/rubber membranes. Existing DEM models

that consider flexible membrane can be classified into four categories: stacked walls method [8-11], periodic boundary [12], equivalent force algorithms [7, 13-15], and particle membrane method [5, 16-20].

2.1 Stacked walls

The main idea of the stacked walls method is that the membrane is constituted of a number of stress-controlled rigid planar walls. These planar walls can deform independently of one another and their velocities are determined by a numerical servo algorithm to maintain the prescribed confining stresses. The method was initially reported by Zhao and Evans [9, 11], and later Ergenzinger *et al.* [8] reported a similar simulation method. Khoubani and Evans [10] improved the deformable ability of stacked-wall boundary further. This method is conceptually simple and easy to be implemented. Li *et al.* [21, 22] applied the method to the simulation of torsional shear testing. However, this approach also has unavoidable disadvantages: 1) it is incapable of characterising the "clamped effects" at the two ends of the triaxial sample (see the illustration of the effect in Fig. 1), and thus affects stress distribution and shape configurations during testing; and 2) the real deformation behaviour of the membrane during triaxial testing is stretch-dominated, while the rigid-wall boundary is equivalent to having an infinitely large stiffness and does not allow elastic deformation, thus it cannot reproduce the influences of membrane properties.

2.2 Periodic boundary condition

The periodic boundary condition (PBC) is used to reduce the computation scale of a large (or infinite) model or eliminate the boundary effects of simulations [23]. Its application in DEM simulation of triaxial tests can be traced back to Cundall [24]. A

periodic boundary always has an exact copy on the opposite side. Particles that move out of a periodic boundary will re-appear back to the sample space with the same velocity from the opposite boundary. Therefore, a numerical model with PBC is assumed to be infinite in the direction normal to the boundaries [12]. The infinite domain is approximated in the sense that it can be characterised by repeated representative volume elements or RVEs. As the physical nature of a PBC differs from a physical latex membrane, the PCB technique exhibits the following problems: 1) models with PBC may not be able to correctly characterise some boundary deformation in triaxial samples (e.g. dilating boundary) [25], so that the volume strain of the model with PBC may be different from a physical sample [24]; 2) it is hard to capture localised shear bands accurately, as the periodic boundary eliminates the effects of local boundary locations with concentrated deformation or stress [24]; and 3) it is difficult to maintain a stable confining stress when a large shear strain occurs [12].

2.3 Equivalent force algorithms

The membrane works by applying forces on the outmost particles of the specimen that are in touch with the membrane during triaxial testing. By calculating the equivalent force arising from the membrane and imposing on the outmost particles, the flexible boundary can be replaced numerically. This method contains two critical procedures: 1) identification of the outmost particles; and 2) calculation of the equivalent confining forces. Since introduced by Bardet and Proubet [26] in DEM modelling of triaxial testing, different algorithms solving these two procedures are proposed [7, 13-15, 19, 27-29]. Particularly, Cheung and O'Sullivan [13] extended this method by using the Voronoi polygon projection technique. However, these algorithms also have some disadvantages: 1) the effects of membrane properties, such

as elastic modulus and thickness on the mechanical response of the test specimen cannot be properly considered; and 2) the "clamped effects" at the two ends of the triaxial sample cannot be reproduced, but the reinforcement arising from "clamped effects" cannot be ignored.

2.4 Bonded-particle membrane

Membrane can be modelled by bonded particles in DEM, namely bonded-ball membrane. This method applies confining forces on particles but is fundamentally different from the equivalent force algorithms, as the membrane itself is modelled in the former while the latter ignores the existence of latex membrane.

The practice of simulating a flexible boundary by bonded particles has long been proposed [30]. Iwashita et al [31] applied this scheme to biaxial simulation. After the implementation on triaxial modelling was reported by Bono and McDowell [16], the bonded-ball method was later used in a few studies [32-34]. Furthermore, Lu *et al* [17] improved the deformability of membrane by extending the size of the membrane. Cil and Alshibli [18], and Li *et al* [20] improved the algorithms on applying the hydrostatic confining pressure.

Although this ball membrane method has the potential to take account of properties of a latex or rubber membrane, the current algorithms still suffer from problems, such as a reliable numerical representation for the deformation properties of a real membrane. In addition, it is not clear how the boundary condition will affect the responses of the specimen under triaxial loading.

3 The proposed framework of improved membrane representation

3.1 Geometrical arrangement

Membrane is a continuous material, but bonded particles are not. Thus a deficiency of the ball membrane method is that the represented membrane surface is not sufficiently smooth. There are two possible ways to partially resolve this issue: 1) to use the closest particle arrangement pattern, i.e. one-layer hexagonal packing to represent a membrane; and 2) to make the radius of the equal-sized membrane balls less than those of particles for the specimen. Saussus and Frost [35] experimentally obtained the sand-membrane contact patterns during triaxial testing, according to *n*-nearest-neighbour analysis of sand-membrane contact points (The *n*-nearest-neighbour distance of a point is defined as the average distance between the point and the *n* nearest points). They found that the side length of the hexagonal contact pattern (with the 6-nearest-neighbour distance) is approximately between 16% and 57% greater than the d_{50} of specimen particles (namely 1.16~1.57d_{50}). Thus the size of membrane particles has a limited effect on the sand-membrane contact pattern, if the particle size constituting the membrane is properly selected. Considering the computational costs, the size of membrane particles is selected to be around 1/3 of sample particles based on existing empirical reports [16].

3.2 Boundary condition

One of essential features for triaxial cells is that the flexible membrane is attached to a cap at the top and a pedestal at the bottom using either rubber o-rings, or a rubber band that is wrapped around and thus is restrained at both ends. The constraint of the membrane when the triaxial specimen is subject to the confining stress is called "clamped effects". To reproduce this feature, the radial horizontal displacements at the two ends of the membrane have to be fixed.

3.3 The determination of membrane parameters

3.3.1 Bond strength

As pointed by many researchers [36, 37], thin membranes are stretching-dominated and the bending stiffness can be reasonably ignored. Therefore, the linear bonded contact model was introduced for modelling a bonded-ball membrane, as it enables particles to undergo tensile forces but do not transfer moment. This linear bonded model allows tensile forces to develop until a critical force failure criterion is met in the normal and/or shear directions. Assuming that the membrane is linearly elastic, the tensile strength should be set sufficiently large to accommodate all possible deformations of the membrane during triaxial shearing. In the presence of contact bonds, no friction between bonded particles is present for the flexible boundaries, thus avoiding unnecessary energy loss of the membrane. The deformation of the membrane is completely controlled by the stretch strain.

3.3.2 The density

The density of a real membrane is trivial for triaxial testing, but the stiffness and mass of a particle are two dominant parameters for determining the critical time step used in DEM. As the contact stiffness is controlled by the elastic properties of the equivalent continuum membrane, artificially determining the density of the simulated membrane can be considered from the perspective of numerical efficiency.

3.3.3 The stiffness

The accurate characterisation of deformation for the membrane is critical for establishing a successful model. Inspired by the work of Griffths and Mustoe [38], the elastic parameters of a physical membrane can be used to determine the contact

stiffness of numerical membrane particles based on the equivalence of strain energy. The detailed derivation will be introduced in the next section.

4 Deformation parameters for bonded-ball membrane

In order to make a reasonable approximation, the stiffness parameters (K_n, K_s) for bonded particles cannot be chosen arbitrarily, but must be determined according to the elastic parameters (E and ν) of the continuum membrane.

4.1 Representative unit cell for ball membrane

The fundamental idea of matching micro-particle parameters and macro membrane parameters is the equivalence of strain energy stored in a unit cell and the corresponding area of the membrane [39]:

$$U_{cell} = U_{mem} \tag{1}$$

The criterion for choosing a unit cell is that it can repeat itself in space and restore the original particle packing. This unit cell should be sufficiently large to contain enough structural details (being able to represent the whole model), but should be small enough to enable it to be easily analysed. With these considerations in mind, a hexagonal cell was chosen as the unit cell (Fig. 2). A similar representative cell was also used in [38, 40, 41]. Each particle has a corresponding unit cell and only contacts with its 6 next neighbouring particles (or 6 unit cells).

Considering two bonded particles as shown in Fig. 3, a local (or rotated) coordinate system x_1', x_2', x_3' is chosen where the x_2' is oriented along the link connecting the geometry centres of the two particles. Each particle has six local degrees of freedom (DOF): three translational DOFs (u_1', u_2', u_3'), representing the relative position change

of the two particle centres; and three angular rotations around the centre (u_4', u_5', u_6'). It should be noted that the topology of a particle assembly is independent of the rotation of particles, and thus only displacements in both normal and tangential contact directions are responsible for changes in strain energy of the equivalent continuum [38]. Assuming that the energy stored in each contact is distributed equally to two contacting particles, the total energy stored in a unit cell is:

$$U_{cell} = \frac{1}{4}\sum_{c=1}^{6}\left(\boldsymbol{F}_n' \bullet \boldsymbol{\Delta u}_{\boldsymbol{n}}' + \boldsymbol{F}_{\boldsymbol{s}}' \bullet \boldsymbol{\Delta u}_s'\right) \tag{2}$$

where $\boldsymbol{\Delta u}_{\boldsymbol{n}}'$ and $\boldsymbol{\Delta u}_{\boldsymbol{s}}'$ denote the normal and tangential relative displacements of two contacting particles, respectively, and will be derived in Section 4.2.

Under the small deformation assumption, the relationship between interaction forces and relative displacements of two bonded particles can be written in the linear form. Then Equation (2) can be re-written as:

$$U_{cell} = \frac{1}{4}\sum_{c=1}^{6}\left(K_n \boldsymbol{\Delta u}_n' \bullet \boldsymbol{\Delta u}_{\boldsymbol{n}}' + K_s \boldsymbol{\Delta u}_{\boldsymbol{s}}' \bullet \boldsymbol{\Delta u}_s'\right) \tag{3}$$

4.2 Strain energy formulation based on the relative displacement of particles

The relationship between the relative displacement of particles Δu (global coordinate) and the equivalent strain $\boldsymbol{\varepsilon}$ in continuum was determined by letting the particle displacements of the lattice be equal to the displacements of the corresponding points in the continuum when deformed

$$\Delta u_i = \varepsilon_{ij}^{AB}(x_j^{(B)} - x_j^{(A)}) \tag{4}$$

where $x_j^{(A)}$ and $x_j^{(B)}$ are the coordinates of particles A and B along the x_j direction, ε_{ij}^{AB} is the equivalent strain between particles A and B.

As the local coordinate frame is chosen to make the local x_2' direction oriented

along the link connecting particles A and B, it has:

$$x_j^{(B)} - x_j^{(A)} = L_{AB} l_{2j} \tag{5}$$

where L_{AB} is the distance between the two particles, and l_{2j} is the cosine angle between the x_2' direction in the local coordinate system and the x_j direction in the global coordinate system.

To link the relative displacement Δu_i in the global coordinate with the relative displacement $\Delta u_i'$ in the local system, the following coordinate transformation is conducted:

$$\Delta u_i' = \Delta u_j l_{ji} = \varepsilon_{jk}^{AB} (x_k^{(B)} - x_k^{(A)}) l_{ji} = \varepsilon_{jk}^{AB} L_{AB} l_{2k} l_{ji} \tag{6}$$

where l_{ji} is the cosine angle between the global and local coordinate axes:

$$l_{ji} = \cos\left(e_j', e_i\right) \tag{7}$$

in which e_i is the basis vector along the x_i direction in the global coordinate system, and e_j' is the basis vector along the x_j' direction in the local coordinate system.

The normal relative displacement $\boldsymbol{\Delta u_n'}$ can thus be easily derived as

$$\boldsymbol{\Delta u_n'} = \Delta u_2' = \Delta u_i l_{2i} = \varepsilon_{jk}^{AB} (x_j^{(B)} - x_j^{(A)}) l_{2i} = \varepsilon_{jk}^{AB} L_{AB} l_{2j} l_{2i} \tag{8}$$

While the tangential relative displacement $\boldsymbol{\Delta u_s'}$ can be written as

$$\boldsymbol{\Delta u_s'} = \Delta u_i' - \boldsymbol{\Delta u_n'} = \Delta u_1' + \Delta u_3' = \Delta u_i l_{1i} + \Delta u_i l_{3i} = \varepsilon_{jk}^{AB} (x_j^{(B)} - x_j^{(A)}) \left(l_{3i} + l_{1i}\right) = \varepsilon_{jk}^{AB} L_{AB} l_{2j} \left(l_{1i} + l_{3i}\right) \tag{9}$$

Substituting Equations (9) and (10) into (3), the energy stored in a unit cell can be rewritten as

$$U_{cell} = \sum_c^6 U^c = \frac{{L_c}^2}{4} \sum_c^6 \left[K_n \varepsilon_{ij}^c l_{2j} l_{2i} \varepsilon_{kl}^c l_{2k} l_{2l} + K_s \varepsilon_{ij}^c l_{2j} \left(l_{1i} + l_{3i}\right) \varepsilon_{kl}^c l_{2l} \left(l_{1k} + l_{3k}\right) \right] \tag{10}$$

where L_c, ε_{ij}^c and U^c are the contact distance, equivalent strain, and equivalent strain

energy for each contact *c* (the contact that connects the central particle to each surrounding particle in the unit cell as shown in Fig. 2), respectively.

4.3 Strain energy density

To determine the strain energy density, the volume of the unit cell V_{cell} must be computed. In Fig. 2, any zone connecting two neighbouring nodes represents one third of the equilateral triangle, so the area of each unit cell is

$$v = 2\sqrt{3}r^2 \tag{11}$$

where *r* is the radius of bonded membrane particles;

Assuming that the thickness of the membrane always equals to *t*, then the volume V_{cell} of the unit cell should be:

$$V_{cell} = 2\sqrt{3}tr^2 \tag{12}$$

If the distance between two particles equals two times of the ball radius ($L_c = 2r$), then the stain energy density is:

$$u_{cell} = \frac{U_{cell}}{V_{cell}} = \frac{\sqrt{3}}{6t}\sum_{c}^{6}\left[K_n\varepsilon_{ij}^{c}l_{2j}l_{2i}\varepsilon_{kl}^{c}l_{2k}l_{2l} + K_s\varepsilon_{ij}^{c}l_{2j}\left(l_{1i}+l_{3i}\right)\varepsilon_{kl}^{c}l_{2l}\left(l_{1k}+l_{3k}\right)\right] \tag{13}$$

4.4 Stress and elastic tensor in membrane

By assuming that the corresponding strain field in the unit cell is uniform, a local strain equals to the overall strain in the unit cell ($\varepsilon_{ij} = \varepsilon_{ij}^{c}$). According to theory of elasticity [6], the stress tensor of a continuum can be obtained by differentiating the strain energy density with respect to the corresponding strain component as follows:

$$\sigma_{ij} = \frac{\partial u_{cell}}{\partial \varepsilon_{ij}} = \frac{1}{V}\frac{\partial\left(\sum_{c}^{6}U^{c}\right)}{\partial\varepsilon_{ij}} = \frac{1}{V}\sum_{c}^{6}\frac{\partial U^{c}}{\partial\varepsilon_{ij}} = \frac{1}{V}\sum_{c}^{6}\frac{\partial U^{c}}{\partial\varepsilon_{ij}^{c}} = \frac{\sqrt{3}}{3t}\sum_{c}^{6}\left[K_n l_{2j}l_{2i}\varepsilon_{kl}^{c}l_{2k}l_{2l} + K_s l_{2j}\left(l_{1i}+l_{3i}\right)\varepsilon_{kl}^{c}l_{2l}\left(l_{1k}+l_{3k}\right)\right] \tag{14}$$

The elastic stiffness tensor can be obtained by differentiating the stress component

with respect to the corresponding strain component:

$$C_{ijkl}=\frac{\partial\sigma_{ij}}{\partial\varepsilon_{kl}}==\frac{1}{V}\sum_{c}^{6}\frac{\partial^2U^c}{\partial\varepsilon_{ij}^c\partial\varepsilon_{kl}^c}=\frac{\sqrt{3}}{3t}\sum_{c}^{6}\left[K_n l_{2j}l_{2i}l_{2k}l_{2l}+K_s l_{2j}\left(l_{1i}+l_{3i}\right)l_{2l}\left(l_{1k}+l_{3k}\right)\right] \quad (15)$$

4.5 Stiffness tensor for ball membrane

For the case that the radius of the cylindrical membrane for enclosing the triaxial specimen far outweighs that of bonded particles constituting the membrane, the unit cell involving 6 contacts can be viewed as a plane. In our model described in Fig. 3, the local coordinate frame (x_i') is obtained by changing the coordinate axes in the global coordinate frame (x_i). Specifically, the x_1 axis remains unchanged, and x_2 and x_3 always rotate the same angle, so that the direction cosine l_{ij} can be obtained as

$$\begin{bmatrix} l_{11} & l_{12} & l_{13} \\ l_{21} & l_{22} & l_{23} \\ l_{31} & l_{32} & l_{33} \end{bmatrix}=\begin{bmatrix} 1 & 0 & 0 \\ 0 & \cos\left(e_2',e_2\right) & \sin\left(e_2',e_2\right) \\ 0 & -\sin\left(e_2',e_2\right) & \cos\left(e_2',e_2\right) \end{bmatrix}=\begin{bmatrix} 1 & 0 & 0 \\ 0 & c & s \\ 0 & -s & c \end{bmatrix} \quad (16)$$

For a general elastic material, considering the symmetry condition of elastic component C_{ijkm}, a shorter matrix notation for the elastic matrix form is written as:

$$\boldsymbol{C}=\begin{bmatrix} C_{1111} & C_{1122} & C_{1133} & 0 & 0 & 0 \\ C_{2211} & C_{2222} & C_{2233} & 0 & 0 & 0 \\ C_{3311} & C_{3322} & C_{3333} & 0 & 0 & 0 \\ 0 & 0 & 0 & \frac{C_{2332}+C_{2323}}{2} & 0 & 0 \\ 0 & 0 & 0 & 0 & \frac{C_{1313}+C_{1331}}{2} & 0 \\ 0 & 0 & 0 & 0 & 0 & \frac{C_{1212}+C_{1221}}{2} \end{bmatrix} \quad (17)$$

Substituting Equations (16) and (17) into (18) leads to

$$\boldsymbol{C}=\frac{\sqrt{3}}{4t}\begin{bmatrix}0 & 0 & 0 & 0 & 0 & 0\\ 0 & 3K_n+K_s & K_n-K_s & 0 & 0 & 0\\ 0 & K_n-K_s & 3K_n+K_s & 0 & 0 & 0\\ 0 & 0 & 0 & K_n+K_s & 0 & 0\\ 0 & 0 & 0 & 0 & 2K_s & 0\\ 0 & 0 & 0 & 0 & 0 & 2K_s\end{bmatrix} \tag{18}$$

Assuming that the response of the membrane in the plane x_2-x_3 is isotropic, the bonded-ball membrane can be regarded as a transversely isotropic material. It follows that the constitutive relationship matrix can be expressed in terms of engineering constants E, v, and G as follows:

$$\begin{bmatrix}\varepsilon_{11}\\ \varepsilon_{22}\\ \varepsilon_{33}\\ \varepsilon_{23}\\ \varepsilon_{31}\\ \varepsilon_{12}\end{bmatrix}=\begin{bmatrix}\frac{1}{E_1} & -\frac{\nu_1}{E_1} & -\frac{\nu_1}{E_1} & 0 & 0 & 0\\ -\frac{\nu_1}{E_1} & \frac{1}{E_2} & -\frac{\nu_2}{E_2} & 0 & 0 & 0\\ -\frac{\nu_1}{E_1} & -\frac{\nu_2}{E_2} & \frac{1}{E_2} & 0 & 0 & 0\\ 0 & 0 & 0 & \frac{1}{2G_2} & 0 & 0\\ 0 & 0 & 0 & 0 & \frac{1}{2G_1} & 0\\ 0 & 0 & 0 & 0 & 0 & \frac{1}{2G_1}\end{bmatrix}\begin{bmatrix}\sigma_{11}\\ \sigma_{22}\\ \sigma_{33}\\ \sigma_{23}\\ \sigma_{31}\\ \sigma_{12}\end{bmatrix} \tag{19}$$

For the proposed bonded-ball membrane, the thickness of the membrane is assumed unchanged when subjected to potential stress conditions, namely $E_1=\infty$. Therefore, Equation (20) can be expressed as:

$$\begin{bmatrix}\varepsilon_{11}\\ \varepsilon_{22}\\ \varepsilon_{33}\\ \varepsilon_{23}\\ \varepsilon_{31}\\ \varepsilon_{12}\end{bmatrix}=\begin{bmatrix}0 & 0 & 0 & 0 & 0 & 0\\ 0 & \frac{1}{E} & -\frac{\nu}{E} & 0 & 0 & 0\\ 0 & -\frac{\nu}{E} & \frac{1}{E} & 0 & 0 & 0\\ 0 & 0 & 0 & \frac{1}{2G_2} & 0 & 0\\ 0 & 0 & 0 & 0 & \frac{1}{2G_1} & 0\\ 0 & 0 & 0 & 0 & 0 & \frac{1}{2G_1}\end{bmatrix}\begin{bmatrix}\sigma_{11}\\ \sigma_{22}\\ \sigma_{33}\\ \sigma_{23}\\ \sigma_{31}\\ \sigma_{12}\end{bmatrix} \tag{20}$$

where $E=E_1=E_2$ and $v=v_1=v_2$, correspond to the elastic modulus and Poisson ratio in the isotropic plane. Without involving ε_{11} and σ_{11}, the stiffness matrix can be reduced to

$$\begin{bmatrix}\sigma_{22}\\ \sigma_{33}\\ \sigma_{23}\\ \sigma_{31}\\ \sigma_{12}\end{bmatrix}=\begin{bmatrix}\frac{1}{E} & -\frac{\nu}{E} & 0 & 0 & 0\\ -\frac{\nu}{E} & \frac{1}{E} & 0 & 0 & 0\\ 0 & 0 & \frac{1}{2G_2} & 0 & 0\\ 0 & 0 & 0 & \frac{1}{2G_1} & 0\\ 0 & 0 & 0 & 0 & \frac{1}{2G_1}\end{bmatrix}^{-1}\begin{bmatrix}\varepsilon_{22}\\ \varepsilon_{33}\\ \varepsilon_{23}\\ \varepsilon_{31}\\ \varepsilon_{12}\end{bmatrix}=\begin{bmatrix}\frac{E}{1-\nu^2} & \frac{E\nu}{1-\nu^2} & 0 & 0 & 0\\ \frac{E\nu}{1-\nu^2} & \frac{E}{1-\nu^2} & 0 & 0 & 0\\ 0 & 0 & 2G_2 & 0 & 0\\ 0 & 0 & 0 & 2G_1 & 0\\ 0 & 0 & 0 & 0 & 2G_1\end{bmatrix}\begin{bmatrix}\varepsilon_{22}\\ \varepsilon_{33}\\ \varepsilon_{23}\\ \varepsilon_{31}\\ \varepsilon_{12}\end{bmatrix} \tag{21}$$

By comparing the stiffness matrixes of the elastic membrane between Equations (19) and (22), we can derive:

$$\frac{\sqrt{3}\left(3K_n+K_s\right)}{4t}=\frac{E}{(1-\nu^2)} \tag{22}$$

$$\frac{\sqrt{3}\left(K_n-K_s\right)}{4t}=\frac{E\nu}{(1-\nu^2)} \tag{23}$$

Thus the relation between the contact stiffnesses of bonded balls in the hexagonal pattern and its equivalent elastic continuum can be expressed as

$$\begin{cases} K_n = \dfrac{Et}{\sqrt{3}(1-\nu)} \\ K_s = \dfrac{Et(1-3\nu)}{\sqrt{3}(1-\nu^2)} \end{cases} \tag{24}$$

The above derived formula can be applied to determine the contact stiffness in the whole membrane.

4.6 Verification of bonded-ball membrane

Several uniaxial tension tests were conducted to validate the proposed bonded ball membrane. The numerical results were compared with the analytic solution derived from classical elastic mechanics.

Taking a triaxial specimen with a height of 98mm, a cylindrical radius of 25mm and a membrane particle radius of 0.001mm as an example, the uniaxial tension cases for membrane was performed. Consider the cylindrical membrane subject to a vertical tensile force on the two ends of the numerical membrane, and assume that the membrane is lineally elastic. From the perspective of elastic mechanics, the extension subjected to an axial force F can be expressed as:

$$\Delta l = \frac{FL}{EA} \tag{25}$$

where E, L, A are the elastic modulus, length and sectional area of the membrane, respectively.

The particle radius constituting the membrane bears resemblance with the element size in FEM or FDM. A finer discretisation will achieve a more accurate solution. The ball representation for a membrane, however, has another issue: the particle number constituting each line or column must be an integer and thus a random radius probably lead to some differences in membrane arrangement. Performing several sets of uniaxial tension tests with increasing the ratio of the cylindrical radius to the radius of

particles constituting the membrane, the analytical solution from Equation (24) was compared with the DEM numerical solution based on the derived particle-scale parameters from Equation (23), as shown in Fig. 5. The results show that the errors are less than 5% when the radius ratio between the cylindrical membrane and the membrane particles is larger than 35. The general agreement also demonstrates that the bonded-ball membrane is a reliable approximation to the elastic behaviour of membrane.

Although no clear pattern can be found, an empirical rule to determine a radius range of membrane particles can still be proposed. When the radius ratio is less than 35, which leads to a coarse discretisation, the numerical error may be unsatisfactorily large. When the radius ratio is over 100, the resulting particle system may have too many elements, giving rise to practically unaffordable computation costs. Therefore, the radius ratio ranging between 35 and 100 appears to strike a reasonable balance between accuracy and computational cost.

5 Implementation of bonded-ball membrane on triaxial testing

5.1 The implementation steps of bonded-ball membrane

The triaxial specimen and ball membrane tend to be generated by two methods [32]. One generates the specimen and the membrane independently, and is called the “step-by-step membrane forming method”. Another method is the “once membrane-forming method”, which generates the specimen and the membrane at the same time. The latter method develops the predefined confining stress by relocating positions of membrane particles. The initial hexagonal packing configuration of membrane particles probably becomes disordered and the accuracy of parameter equivalence (macro and meso) can be compromised by the disordered packing configuration.

Therefore, the first “step-by-step membrane forming method” is considered here.

The first step of the method is to generate a specimen within a cylindrical wall and load the specimen to the predefined confining stress by using the conventional servo-wall method.

Having prepared a specimen roughly within the predefined stress and geometric condition, the bonded-ball membrane is then installed in the second step based on the following sub-steps: 1) Set all linear and rotational velocities of the specimen particles to 0; 2) Delete the original lateral wall boundary; 3) Install the hexagonal ball membrane (Note the radius of the cylindrical membrane should be slightly larger than the rigid wall boundary considering the volume of membrane particles. Empirically, this gap may be 0.9-0.95 times of the radius of the membrane ball); and 4) Deactivate the contact interaction between the membrane and the loading wall.

After the bonded-ball membrane has been installed, the loading of the confining pressure is implemented based on the following sub-steps: 1) Fix the velocity of the bonded particles; 2) Release the velocity of the specimen and iterate the whole system to a rough state of equilibrium; 3) Assign external forces on the bonded ball membrane (This step corresponds to the experimental step of loading hydrostatic pressure on the membrane. The main idea of assigning external forces follows the contribution of [20] and will be briefly introduced in Section 5.2); 4) Release the velocity of the bonded-ball locating between the top and bottom loading plates and fix the membrane particles outside the top and bottom loading plates to reproduce the clamped effects as the experiment does; and 5) iterate the model to a state of equilibrium.

The axial loading is simulated by giving an identical speed on both loading plates and the membrane particles outside them. The loading rate should be slow enough to

maintain a quasi-static condition.

5.2 The implementation of confining stress condition

The hydrostatic pressure is characterised by isotropic stress, so the critical point for the implementation of confining stress consists in exerting static forces uniformly in all orientations. With the hexagonal ball packing, the whole membrane can be viewed as being discretised into a set of triangular networks, as illustrated in Fig. 2a. The hydrostatic force exerted on each triangle can be assumed to be shared equally among the three balls that constitute the triangle. Then the resultant force acting on each particle can be computed from the 6 neighbouring particle triangles. For example, the total force $\boldsymbol{F}^{\boldsymbol{0}}$ acting on particle 0, illustrated in Fig. 2b, is:

$$\boldsymbol{F}^{\boldsymbol{0}} = \frac{\sigma_{static}}{3} \sum_{i}^{6} \boldsymbol{n_i} S_i \tag{26}$$

where σ_{static} is the confining stress; $\boldsymbol{n_i}$ and S_i are the normal direction and area of the i^{th} triangle, respectively.

Both horizontal and vertical confining stresses can be considered in the above formulation. As all the coordinates for membrane particles are known, the total force shared by each particle can be determined. Furthermore, the directions of the confining pressure can be updated after every few cycles to fit the possible deformation of the triaxial specimen. This means that the confining pressure can be accurately characterised even the shape of the specimen undergoes a large deformation.

5.3 Volume calculation for sample with flexible boundary

Another problem arising from particle membrane is the determination of the

specimen volume. The volume of a deformed specimen with a bonded-ball membrane representation is not as straightforward as for the specimen with a rigid boundary. Here several effective methods are provided.

The first method is based on the Gauss divergence theorem [20]. The idea is that the specimen is bounded by the surface triangles (of the flexible membrane) and the loading planes (both top and bottom), and thus it can be viewed as a closed space. Then the volume calculation of the whole specimen can be simplified to the integrals of the surface enclosing the specimen. For each surface triangle, their vertex coordinates are the corresponding coordinates of membrane particles, and then their outward normal can be easily determined by the known positions. By using the Gauss theorem, the volume of specimen can be obtained:

$$V_s = \iiint_v dV = \oiint_S \boldsymbol{x}_1^c \bullet \boldsymbol{n}_1^c dS \approx \sum_{c \in V} x_1^c n_1^c A^c \tag{27}$$

where V_s is the volume of the specimen; S is the surface of the closed specimen space(including the top and bottom loading plates). For the i^{th} triangle (or element) c on the membrane surface, the centroid coordinate $\boldsymbol{x}_i^c = (x_1^c, x_2^c, x_3^c)$, the outward normal $\boldsymbol{n}_i^c = \left(n_1^c, n_2^c, n_3^c\right)$, A^c is the area of corresponding triangle or element c.

The second method is called the radial polyhedron. As the membrane can be fully represented by a set of triangulated elements, a tetrahedron can always be generated by connecting an arbitrary point inside the specimen and the three vertices of an arbitrary surface triangle. The volume of each tetrahedron can be simply computed. Then the volume of the specimen can be given as follows:

$$V_s = \frac{1}{3} S_{end} h + \sum_s \frac{\left|\left(\boldsymbol{a}_i \times \boldsymbol{b}_i\right) \bullet \boldsymbol{c}_i\right|}{6} \tag{28}$$

where S_{end} is the contact area between the top or bottom platen and the specimen; h is

the height of the triaxial specimen; $\boldsymbol{a_i}$, $\boldsymbol{b_i}$, and $\boldsymbol{c_i}$ are three vectors connecting a point inside the specimen and the three vertices of the i^{th} surface triangle, respectively.

The last method is to use the Voronoi tessellation [42]. The Voronoi tessellation enables each particle within specimen to be uniquely assigned a polyhedral volume. The sum of all polyhedral volumes will be the volume of the specimen.

As the deformation of a triaxial specimen takes place incrementally during testing, the logarithmic strain (also called true strain or Hencky strain) was adopted to consider the influence of the strain path. In this study, the axial strain ε_1 and volumetric strain ε_v are given as follows [43]:

$$\varepsilon_1 = -\int \delta\varepsilon = -\int_{H_0}^{H} \frac{\delta H}{H} = -\ln\left(\frac{H}{H_0}\right) = \ln\left(\frac{H_0}{H}\right) \tag{29}$$

$$\varepsilon_V = -\int \delta\varepsilon_V = -\int_{V_0}^{V} \frac{\delta V}{V} = -\ln\left(\frac{V}{V_0}\right) = \ln\left(\frac{V_0}{V}\right) \tag{30}$$

where H and V are their current height and volume of the specimen, respectively, and H_0 and V_0 are respectively the initial height and volume of the specimen before testing. Note the compression is assigned a positive value.

6 Triaxial testing

6.1 Triaxial testing configuration for DEM simulation and experiment

To verify the effectiveness of the proposed bonded-ball membrane, two sets of triaxial testing simulations were performed based on the reported laboratory experiments [18]. Table 1 summarises the experiment data, and Table 2 lists the corresponding membrane and specimen parameters. A set of common elastic parameters for latex membrane were selected (the elastic modulus is 1.25 MPa, the Poisson ratio is 0.2, and the membrane thickness is 0.3mm). The corresponding

particle-scale parameters are determined based on Equation (25) and can be found in Table 2.

The step-by-step procedures for making a specimen enclosed with a flexible membrane can be referred to Section 5.1. After having prepared the triaxial specimen with the predefined confining stress, the specimen was loaded by moving both the top and bottom plates simultaneously towards each other at a rate of 0.05m/s, which has been checked to be slow enough to ensure a quasi-static condition. When the axial strain reaches 16%, the triaxial loading process terminates.

6.2 Stress-strain relation

The stress-strain relationship for soils is fundamental to understand their mechanical behaviours such as the strength and stiffness. As particle packing configurations in experiments cannot be perfectly reproduced in any DEM specimen, some mechanical behaviour of granular assemblies therefore will inevitably be influenced by some random factors. To obtain meaningful comparisons, numerical tests with two different random seeds (R1 and R2) are performed to show the sensitivity due to random packing.

Figure 6a compares stress-strain responses obtained from experimental data and DEM simulations with the flexible membrane boundary (T1 and T2 represent confining stresses of 50kPa and 100kPa, respectively). It shows that the proposed membrane algorithm is generally reliable in reproducing the experimental outputs. Fig6b shows comparison of stress-strain responses arising from triaxial testing with both flexible membrane and rigid-wall boundary, respectively. To make the data clearer, and to further understand the influence of confining stress, two groups of additional tests (T3) with a higher confining stress (200 kPa) were added in Fig.6b.

It is evident that the discrepancies of the results due to different boundary conditions are comparable with those due to random variations in packing. Thus it can be concluded that the boundary condition may have limited impacts on the stress-strain responses of granular materials, especially in the initial elastic zone of stress-strain curves. However, it is still observed that models with a rigid wall boundary slightly underestimate the deviator stress in the post-elastic zone compared to the simulations with a flexible membrane boundary. Similar conclusions are obtained in [10, 18-19]. The mechanism responsible for this difference is that the end restraint in our models with the flexible boundary acts as an additional confinement at the ends of the specimen, preventing the soil from moving outwards freely. In the elastic zone, the packing structure and particle stiffness play dominant roles in determining the initial stress-strain curves, but in the post-elastic zone, the restraints of lateral deformation at the two ends of the specimen (including end friction) may reinforce the strength of the specimen. Thus discrete element models with flexible boundaries but without end restraints generally show that the boundary condition has limited influences on the stress-strain behaviour [13].

In the post-peak regime of the stress-strain curves, the specimen with the flexible membrane under 50 kPa always match well with the experimental results, but its counterparts under 100kPa exhibits a softening phenomenon, similar to the other two sets of testing with the rigid boundary. The reason for the softening occurred in the case of 100kPa may be related to the initial particle structure and will be further discussed in Section 6.4. Overall, a generally satisfactory agreement between the laboratory experiment and the numerical results with the flexible membrane boundary demonstrates that the proposed membrane algorithm is reliable.

In addition to the friction and stiffness of a single particle, the density, pre-shear

stress, and soil structure are also critical to determine the shearing resistance of soils [44-46]. For the granular assembly, the homogenisation of density, stress distribution and packing structure within the specimen may be compromised by particulate jamming, where only several strong force chains along the compressional direction bears most of the external load but the weak contacts out of the strong force chains make a practically negligible contribution in terms of resisting the external load [47, 48]. In addition, the loading rate or strain rate also affects the stress-strain relations of granular sand [49-51]. Although no clear explanation is reported, the widely used method by matching the stress-strain curves of sheared granular assembly to calibrate the parameter of a single particle is just a rough reflection for the macro responses.

A recognisable slip-stick phenomenon is experimentally observed, but both DEM models show no such visibly related behaviour. The slip-stick phenomenon tends to be viewed as the production of the evolution of force chains in granular assembly [52]. As the granular assembly transmits external forces in the form of force networks [53], the strain-dominated compression method in triaxial testing will cause the continuous break and reconstruction of force chains. The break or collapse of strong force columns gives rise to a sudden reduction in the stress during compression, but newly developed strong force chains occur as the compression continues, and then the resistance to shear or stress within specimen comes back right away. The difference of particle structures between experiments and numerical models may be another factor that affects the evolution of force chains.

In addition, the mechanism responsible for the slip-stick phenomenon may be related to the behaviour of frictional strength between two sliding interfaces. The sliding of real interfaces between two bodies also tends to show a similar slip-stick phenomenon [54]. The evolution of frictional strength is governed by the real contact

area and the shear strength of contact [55]. Typically, the applied forces on the contact interface are just supported by several micro-contacts comprising only a small part of the apparent contact areas and the shear strength of contacts are rate-dependent. However, the frictional motion is conceptually viewed as the motion in an ideal point contact and is simply described by the Coulomb law in the numerical model. Therefore, the simplified contact model may be another reason for the difference of the slip-stick phenomenon.

6.3 Volume change

A significant feature of soils is that the shear deformation process is accompanied by a change in volume, partly due to the rearrangement of soil particles when subjected to external forces. As a macro index to characterise the whole behaviour of soils, the shear-induced volume change of the specimen with both rigid and flexible boundaries are investigated. The volume strain for the specimen with the membrane boundary is calculated based on Equation (31).

As Fig. 7 shows, all the specimens exhibit the volume contract behavior during the shearing as relatively loose specimens were used, but their stress-strain relations are not necessarily stress hardening. In particular, the triaxial tests with the rigid boundary tend to show softening in the post-peak regime of stress-strain relations.

Under the identical axial strain, the specimens with the membrane boundary show a larger volumetric strain compared with the specimens with the rigid boundary in both confining stress conditions. The volumetric strain of triaxial testing with a flexible boundary is approximately the twice of its counterpart with a rigid boundary. In addition, the volumetric strain in all of the tests show a similar trend and similar values at the initial development stage of axial strain, because the initial axial strain of

triaxial shearing is dominated by the elastic deformation, and the boundary conditions play a lesser role in this stage.

6.4 Failure modes and shear band

The localisation of plastic deformation in the form of shear bands is a common feature for the instability of ductile solid [56]. However, the faillure modes of geological materials under triaxial shearing show not only the brittle failure with shear planes but also the barrelling failure [57, 58]. Bono *et al.* [59] stated that the failure mode of triaxial testing is related to the cementation strength of specimen particles and the confining stress.

In this work, the failure model of triaxial testing is found to be related to the boundary condition. Figure 7 depicts the deformation of the triaxial specimen with both flexible and rigid boundaries after sheared to a final axial strain of 16%. The specimen with the rigid boundary always keeps a cylindrical shape, as the particles within the specimen are forced to adapt to the kinematics of the boundary walls. However, this is not the case for the flexible boundary. Particles enclosed by the flexible boundary are able to move freely at any position. The specimen shows a barrelling deformation under the confining stress of 50 kPa, and the deformation of the specimen under the confining stress of 100kPa cannot be easily concluded yet but it also shows free movement characteristics clearly.

In a specimen undergoing triaxial loading, the strain near the loading plates is significantly larger than the other parts within the specimen, as the specimen deforms due to the strain-controlled loading. Therefore, the shear band of the triaxial specimen tends to be recognised by non-strain indications such as the particle rotation, the rotation of principal stress, the rotation of principal fabric tensor and displacement

within the specimen subjected to triaxial testing [60, 61].

Figure 8 shows the displacement field of the triaxial specimen sheared to an axial strain of 16%. A highly localised deformation pattern is captured. A slant and band-like shear zone was clearly found in the specimen enclosed with a rigid boundary. The specimens enclosed with a membrane boundary show a slant band-like zone under the confining stress of 100 kPa and a horizontal ring-like zone under the confining stress of 50 kPa. Although the similar slant band-like shear zone was captured in the specimen enclosed with a flexible membrane under the confining stress of 100kPa, the position and orientation of the shear band are different.

The generation of shear band in triaxial testing with a flexible boundary under the confining stress of 100kPa can be explained with the Griffith flaw. As pointed by Rice [56], the localised instability may be in situations that are dominated by some strong local inhomogeneity. There are some local and initial flaws or relatively large voids within the randomly distributed particulate assembly that may cause the initiation of a localised zone and subsequently gives rise to concentrating deformation in its vicinity. Particularly, a granular specimen with a relatively small number of particles is easier to be affected by such initial inhomogeneity. As only 2303 particles in total were considered in our current model in order to reduce the computational costs, the present numerical results may not be difficult to match experiments, as actual packing configurations in experiments cannot be perfectly reproduced in DEM specimens; However, by performing the triaxial tests with the same packing configuration but with different boundary conditions, it is shown that different boundary conditions can give rise to different failure models for a specimen subjected to triaxial shearing.

7 Micro explanation for macro responses with two different boundaries

The macro response tends to have some micro origins for granular assemblies. In this section, the particle-scale quantities, including contact forces and contact fabric, were investigated to understand how boundary conditions affect the micro behaviour of granular materials.

7.1 The distribution of contact forces

Contact forces are the internal resistances or counterforces of a granular assembly when subjected to external forces. The contact force distribution can reveal how the external load is transferred within in a granular assembly. As a straightforward characterisation of contact forces is difficult to achieve in a 3-dimensional model, a statistical analysis is adopted here for estimation and quantitative comparisons [62, 63]. Define strong contacts as their normal contact force above the mean normal force $<f_n>$ within a granular assembly and vice versa for weak contacts. Aze´ma and Farhang Radja¨ [64] proposed a mathematical model to reflect the probability distribution of strong and weak contact forces within a granular assembly subjected to biaxial shearing and found that the probability distribution of strong contacts varies exponentially, whereas the probability distribution of the weak contacts follows a power law.

The logarithmic probability density function (pdf) of normal contact forces normalised by the mean normal force of triaxial tests with a flexible membrane was plotted in Fig. 10. It clearly shows that the boundary condition has a significant effect on the distribution of contact forces. Particularly, the probability distribution of strong contacts for triaxial shearing tests with a rigid boundary is evidently larger than those with a flexible boundary. From the fitted curves of the probability distribution for all

triaxial cases, strong and weak force networks are also dependent on the boundary condition. Furthermore, the confining stresses seem to have very limited influences on the probability density function of normal contact forces.

An interesting phenomenon observed from our simulations is worth mentioning. The specimen with the flexible membrane boundary is much easier to reach the predefined stress condition, while the specimen with the rigid boundary tends to achieve an undesired stress state inside the specimen, even if the servo-stresses condition on the boundary has been satisfied. This phenomenon can be well-explained by the distribution of contact forces. The specimen with a flexible boundary tends to develop well-distributed contact forces, but the one within a rigid boundary generally develops a non-homogeneous distribution of contact forces where some contacts bear excessive contact forces while some contacts share a very limited portion of overall external forces (similar to the jamming phenomenon). This indicates that the boundary condition is also a factor for leading to jamming of a granular assembly.

7.2 Fabric evolution

It is well-known that the spatial arrangement of particles and voids tends to exhibit anisotropy and evolves to a specially preferred orientation during loading, namely the stress-induced anisotropy, because the particle contacts tend to separate in the directions that are approximately orthogonal to the direction of the major principal stress during shear deformation [65, 66]. Fabric refers to the spatial arrangement of particles and associated voids [67]. The initial fabric of granular specimen is an important factor for determining its mechanical behaviour.

The commonly used second-order fabric tensor was characterised with the distribution of contact normal and branch vectors. The mathematical definition of a

second-order fabric tensor is proposed by Oda [68] as follows:

$$\phi_{ij} = \int_{\Omega} n_i n_j E(n) \mathrm{d}\Omega = \frac{1}{N_c} \sum_{k=1}^{N_c} n_i^k n_j^k \tag{31}$$

where N_c is the number of contacts, n_i is the i-direction component of the unit vector along the normal direction of the contact plane, and $E(n)$ is the contact normal distribution function. As shown in Fig.11, Ω is a unit sphere and $d\Omega$ is the differential surface representing the contact plane. The expansion of Equation (32) gives a three-dimensional matrix as:

$$\phi_{ij} = \begin{pmatrix} \phi_{\mathrm{xx}} & \phi_{\mathrm{xy}} & \phi_{\mathrm{xy}} \\ \phi_{\mathrm{xy}} & \phi_{\mathrm{xy}} & \phi_{\mathrm{xy}} \\ \phi_{\mathrm{xy}} & \phi_{\mathrm{xy}} & \phi_{\mathrm{xy}} \end{pmatrix} = \frac{1}{N_c} \begin{pmatrix} \sum_{k=1}^{Nc} n_x^k n_x^k & \sum_{k=1}^{Nc} n_x^k n_y^k & \sum_{k=1}^{Nc} n_x^k n_z^k \\ \sum_{k=1}^{Nc} n_y^k n_x^k & \sum_{k=1}^{Nc} n_y^k n_y^k & \sum_{k=1}^{Nc} n_y^k n_z^k \\ \sum_{k=1}^{Nc} n_z^k n_x^k & \sum_{k=1}^{Nc} n_z^k n_y^k & \sum_{k=1}^{Nc} n_z^k n_z^k \end{pmatrix} \tag{32}$$

For an arbitrary contact K, the normal orientation of the contact plane can be expressed with the angles defined in Fig. 11 as:

$$n^k = \begin{pmatrix} n_x^k \\ n_y^k \\ n_z^k \end{pmatrix} = \begin{pmatrix} \cos\beta^k \sin\gamma^k \\ \sin\beta^k \sin\gamma^k \\ \cos\gamma^k \end{pmatrix} \tag{33}$$

Then the fabric tensor can be expressed as:

$$\phi_{ij} = \frac{1}{N_c} \begin{pmatrix} \sum_{k=1}^{Nc} \cos^2\beta^k \sin^2\gamma^k & \sum_{k=1}^{Nc} \cos\beta^k \sin\beta^k \sin^2\gamma^k & \sum_{k=1}^{Nc} \cos\beta^k \sin\gamma^k \cos\gamma^k \\ \sum_{k=1}^{Nc} \cos\beta^k \sin\beta^k \sin^2\gamma^k & \sum_{k=1}^{Nc} \sin^2\beta^k \sin^2\gamma^k & \sum_{k=1}^{Nc} \sin\beta^k \sin\gamma^k \cos\gamma^k \\ \sum_{k=1}^{Nc} \cos\beta^k \sin\gamma^k \cos\gamma^k & \sum_{k=1}^{Nc} \sin\beta^k \sin\gamma^k \cos\gamma^k & \sum_{k=1}^{Nc} \cos^2\gamma^k \end{pmatrix} \tag{34}$$

The preferred orientations and the magnitude of the structural anisotropy within a granular specimen can indicate the contact intensity in the direction of principal

stresses and can be expressed with the principal fabric components and its corresponding orientations [69]. Similar to the stress tensor and principal stress components, the eigenvalues and eigenvectors of the fabric tensor give the principal fabric components and their orientations. To capture the effect of boundary conditions on the structural evolution of granular assembly, the principal fabric tensors ϕ_{11}, ϕ_{22}, ϕ_{33} were calculated during the whole course of testing, as shown in Fig. 12.

Initially the fabric distributions of four triaxial specimens are roughly isotropic. During the triaxial shearing, the contact orientations tend to be lined with the vertical direction but gradually deviate from the minor principal fabric direction (horizontal direction). The changes of the fabric tensors also show the irreversible plastic deformation (sliding of particles) that develops throughout the shearing process of specimen rather than after shear bands emerge. Furthermore, after the shear-band fully develops, the major principal fabric tensor, at least from the perspective of overall specimen, starts to decrease gradually.

By using the solid angle representation, the contact normal distribution function *E(n)* can be expressed as *E(γ,β)*, and Equation (32) can be rewritten as follows:

$$\phi_{ij} = \int_0^{2\pi} \int_0^{\pi} n_i n_j E(\gamma, \beta) \sin\gamma d\gamma d\beta \tag{35}$$

The contact normal distribution function *E(γ,β)* is determined by the packing structure of the assembly and thus can be of any form. Kanatani [70] and Chang *at al.* [71] derived a Fourier series representation of the distribution function for a particle assembly statistically symmetric about the direction of the vertical direction. Practically, a simple truncated even-order Fourier series is widely used for the approximation:

$$E(\gamma, \beta) = \frac{3(1 + a\cos 2\gamma)}{4\pi(3 - a)} \tag{36}$$

where a is a parameter that is generally ranged from -1 to 1, and can be used as an indication of fabric anisotropy. When a>0, the contact normals of particles within the specimen tend to align with the vertical direction; when a<0, the contact normals tend to concentrate along the horizontal direction. In addition, Equation (37) is independent of β and has the following property:

$$E(\gamma) = E(\gamma + \pi) \tag{37}$$

Yimsir and Soga [66] derived the fabric tensor further by substituting Equation (35) into Equation (36) and evaluating the integral. The resulting new fabric tensor can be described with the single variable a as:

$$\phi_{ij} = \begin{bmatrix} \frac{3a-5}{5(a-3)} & 0 & 0 \\ 0 & \frac{3a-5}{5(a-3)} & 0 \\ 0 & 0 & \frac{-(5+a)}{5(a-3)} \end{bmatrix} \tag{38}$$

By letting the above fabric tensor equal to the corresponding component calculated from the numerical model based on Equation (35), a mathematically overdetermined system of equations (three equations but only one unknown) is obtained. Here the least squared method (LSM) is introduced to find the approximate solution of a. In this method, the parameter a is required to minimise the sum of squares for error (SSE) defined as

$$S(a) = \left[\phi_{xx} - \frac{3a-5}{5(a-3)}\right]^2 + \left[\phi_{yy} - \frac{3a-5}{5(a-3)}\right]^2 + \left[\phi_{zz} + \frac{5+a}{5(a-3)}\right]^2 \tag{39}$$

i.e. the derivative of $S(a)$ with respect to the parameter a must be zero:

$$\frac{dS(a)}{da} = 0 \tag{40}$$

By solving Equation (41), we obtain:

$$a=\frac{15(\phi_{xx}+\phi_{yy}-2\phi_{zz})}{(-8+5\phi_{xx}+5\phi_{yy}-10\phi_{zz})} \tag{41}$$

With the substitution of the fabric tensor calculated from the simulated results based on Equation (35), an approximation value of the parameter *a* can be quantitatively determined. In the present work, we term the parameter *a* as the *anisotropy degree*, as this single parameter can effectively characterise the degree of anisotropy within a three-dimensional granular assembly.

Figure 13 shows the evolution of *a* during the loading and demonstrates the differences between different boundary and stress conditions. Basically, the specimen with a rigid boundary undergoes stronger fabric anisotropy during triaxial shearing under the identical confining stress. In addition, the anisotropy degree is also related to the confining stress: a stronger degree of fabric anisotropy is captured with a higher confining stress.

The evolution of fabric anisotropy is very similar to the changes of the major principal fabric tensor. The position with the highest degree of anisotropy undergoes a larger axial strain over the peak position of stress-strain curves. As the axial strain further develops, the anisotropy appears to decrease gradually in all the triaxial testing cases. The change of fabric anisotropy of triaxial testing shows that the boundary condition has a significant influence on the microstructure of specimens.

8 The effect of membrane thickness

The thickness of membrane has some effects on the behaviour of triaxial specimen, such as the membrane compliance [72], membrane penetration [73], and even liquefaction tests [74]. The thickness of membrane can be simulated by our proposed

numerical procedure. Particularly, the commonly used thicknesses of membrane are 0.3mm, 0.6mm, and 1mm, respectively. Assuming that the elastic modulus and Poisson ratio are respectively 1.25MPa and 0.2 for the latex membrane, the corresponding particle-scale stiffness parameters for the bonded-ball membrane are obtained, according to our derived Equation (25) and are listed in Table 3.

The stress-strain relations for the triaxial tests with different membrane thicknesses are depicted in Fig. 14. Small but recognisable differences can be observed. The results show that vertical stresses tend to have a larger value when the thickness increases. This means that an overestimated strength for the specimen may be obtained for thick membrane boundaries. Henkel and Gilbert [3] also had experimentally obtained a similar conclusion. The reason behind it is that a stronger boundary constraint is provided from the membrane with a larger thickness. Under an identical deformation (strain condition), a stronger constraint of thicker membrane enables the triaxial specimen to bear a larger induced-stress.

In addition to the thickness, the stiffness parameters of the membrane can also be directly determined and numerically considered. The increase in the membrane stiffness has a similar effect as the increase in the thickness of membrane, as the both increases will give rise to increases in particle-scale stiffness parameters of membrane.

9 Conclusion and Discussion

An algorithm has been proposed in the present work to simulate the flexible boundary of triaxial testing in the DEM framework. The actual properties of a physical membrane, such as elastic parameters and thickness can be represented by numerical particle-scale parameters of flexible boundary. Furthermore, the specimen can deform freely with the hydrostatic confining stress from arbitrary directions to be

implemented accurately. The proposed algorithm has been validated with laboratory experiments. Numerical triaxial tests with both flexible and rigid boundaries have also been compared from the meso scale to the macro scale. The results show that the boundary conditions of triaxial testing have limited influences on the stress-strain behaviour but a relatively large impact on the volumetric change, the failure mode, the distribution of contact forces, and the fabric evolution of particles in the specimen during triaxial testing.

Nevertheless, the proposed algorithm deals with the triaxial testing with drained conditions or with dry particles only. For undrained loading cases, one can couple a DEM code with a CFD code to simulate undrained cases [75]. A possible solution is to couple DEM with the lattice Boltzmann method (LBM) [76-78]. Alternatively, one can also use DEM models involving only dry particles to simulate the undrained condition approximately by performing constant-volume shearing [43,66,79]. By adjusting the horizontal strain continuously with the vertical compression, a constant value for the total assembly volume can be maintained during shearing. It is possible to fit the assumption of constant volume during shearing in our model. Particularly, it can be easily implemented if the boundary is assumed to move with a constant rate, although this scheme will make the flexible particle membrane degenerate into a method similar to the rigid wall method. Alternatively, to keep the membrane deformed freely considering the “clamped effects” at the two ends of the triaxial specimen when simulating the undrained condition, a possible solution is to assume a deformation pattern for the membrane (such as barrelling), but it is necessary to verify the approach with a number of laboratory experiments.

ACKNOWLEDGMENTS

Financial supports from the National Natural Science Foundation of China (Grants No. 51579237 & 51779017) are appreciated.

Reference

[1] Frost JD, Evans TM. Membrane Effects in Biaxial Compression Tests. Journal of Geotechnical and Geoenvironmental Engineering. 2009;135(7):986-91.

[2] Newland P, Allely B. Volume changes during undrained triaxial tests on saturated dilatant granular materials. Geotechnique. 1959;9(4):174-82.

[3] Henkel D, Gilbert G. The effect measured of the rubber membrane on the triaxial compression strength of clay samples. Geotechnique. 1952;3(1):20-9.

[4] Vermeer P. The orientation of shear bands in biaxial tests. Geotechnique. 1990;40(2):223-36.

[5] Potyondy DO, Cundall PA. A bonded-particle model for rock. International Journal of Rock Mechanics and Mining Sciences. 2004;41(8):1329-64.

[6] Cheng Y, Nakata Y, Bolton M. Discrete element simulation of crushable soil. Geotechnique. 2003;53(7):633-41.

[7] Wang Y, Tonon F. Modeling triaxial test on intact rock using discrete element method with membrane boundary. Journal of engineering mechanics. 2009;135(9):1029-37.

[8] Ergenzinger C, Seifried R, Eberhard P. A discrete element model predicting the strength of ballast stones. Computers & Structures. 2012;108-109:3-13.

[9] Zhao X, Evans TM. Numerical analysis of critical state behaviors of granular soils under different loading conditions. Granular Matter. 2011;13(6):751-64.

[10] Khoubani A, Evans TM. An efficient flexible membrane boundary condition for DEM simulation of axisymmetric element tests. International Journal for Numerical and Analytical Methods in Geomechanics. 2018;42(4):694-715.

[11] Zhao X, Evans TM. Discrete simulations of laboratory loading conditions. International journal of geomechanics. 2009;9(4):169-78.

[12] Thornton C. Numerical simulations of deviatoric shear deformation of granular media. Géotechnique. 2000;50(1):43-53.

[13] Cheung G, O'Sullivan C. Effective simulation of flexible lateral boundaries in two- and three-dimensional DEM simulations. Particuology. 2008;6(6):483-500.

[14] Cui L, O'Sullivan C, O'Neill S. An analysis of the triaxial apparatus using a mixed boundary three-dimensional discrete element model. Géotechnique. 2007;57(10):831-44.

[15] O'Sullivan C, Cui L. Micromechanics of granular material response during load reversals: Combined DEM and experimental study. Powder Technology. 2009;193(3):289-302.

[16] de Bono J, McDowell G, Wanatowski D. Discrete element modelling of a flexible membrane for triaxial testing of granular material at high pressures. Géotechnique Letters. 2012;2(4):199-203.

[17] Lu Y, Li X, Wang Y. Application of a flexible membrane to DEM modelling of axisymmetric triaxial compression tests on sands. European Journal of Environmental and Civil Engineering. 2018:1-18.

[18] Cil MB, Alshibli KA. 3D analysis of kinematic behavior of granular materials in triaxial testing using DEM with flexible membrane boundary. Acta Geotechnica. 2013;9(2):287-98.

[19] Binesh SM, Eslami-Feizabad E, Rahmani R. Discrete Element Modeling of Drained Triaxial Test: Flexible and Rigid Lateral Boundaries. International Journal of Civil Engineering. 2018.

[20] Li Z, Wang YH, Ma CH, Mok CMB. Experimental characterization and 3D DEM simulation of bond breakages in artificially cemented sands with different bond strengths when subjected to triaxial shearing. Acta Geotechnica. 2017;12(5):987-1002.

[21] Li B, Zhang F, Gutierrez M. A numerical examination of the hollow cylindrical torsional shear test using DEM. Acta Geotechnica. 2014;10(4):449-67.

[22] Li B, Guo L, Zhang F-s. Macro-micro investigation of granular materials in torsional shear test. Journal of Central South University. 2014;21(7):2950-61.

[23] Wang M, Feng Y, Wang Y, Zhao T. Periodic boundary conditions of discrete element method-lattice Boltzmann method for fluid-particle coupling. Granular Matter. 2017;19(3):43.

[24] Cundall P. Computer simulations of dense sphere assemblies. Studies in Applied Mechanics: Elsevier, 1988. p. 113-23.

[25] Kruyt NP, Rothenburg L. Shear strength, dilatancy, energy and dissipation in quasi-static deformation of granular materials. Journal of Statistical Mechanics: Theory and Experiment. 2006;2006(07):P07021.

[26] Bardet J, Proubet J. Numerical investigation of the structure of persistent shear bands in granular media. Geotechnique. 1991;41(4):599-613.

[27] Ng T-T. Triaxial Test Simulations with Discrete Element Method and Hydrostatic Boundaries. Journal of Engineering Mechanics. 2004;130(10):1188-94.

[28] Cui L, O'sullivan C, O'neill S. An analysis of the triaxial apparatus using a mixed boundary three-dimensional discrete element model. Geotechnique. 2007;57(10):831-44.

[29] Wang Y, Tonon F. Modeling Lac du Bonnet granite using a discrete element model. International Journal of Rock Mechanics and Mining Sciences. 2009;46(7):1124-35.

[30] Cundall PA. Numerical experiments on localization in frictional materials. Ingenieur-archiv. 1989;59(2):148-59.

[31] Iwashita K, Oda M. Rolling resistance at contacts in simulation of shear band development by DEM. Journal of engineering mechanics. 1998;124(3):285-92.

[32] Tang H, Zhang X, Ji S. Discrete element analysis for shear band modes of granular materials in triaxial tests. Particul Sci Technol. 2016;35(3):277-90.

[33] Wilson JF, Sáez E. Use of discrete element modeling to study the stress and strain distribution in cyclic torsional shear tests. Acta Geotechnica. 2017;12(3):511-26.

[34] de Bono JP, McDowell GR. DEM of triaxial tests on crushable sand. Granular Matter. 2014;16(4):551-62.

[35] Saussus D, Frost J. Simulating the membrane contact patterns of triaxial sand specimens.

International journal for numerical and analytical methods in geomechanics. 2000;24(12):931-46.

[36] Begley MR, Mackin TJ. Spherical indentation of freestanding circular thin films in the membrane regime. Journal of the Mechanics and Physics of Solids. 2004;52(9):2005-23.

[37] Liu KK, Ju BF. A novel technique for mechanical characterization of thin elastomeric membrane. Journal of Physics D: Applied Physics. 2001;34(15):L91.

[38] Griffiths D, Mustoe GG. Modelling of elastic continua using a grillage of structural elements based on discrete element concepts. International Journal for Numerical Methods in Engineering. 2001;50(7):1759-75.

[39] Ostoja-Starzewski M. Lattice models in micromechanics. Applied Mechanics Reviews. 2002;55(1):35-60.

[40] Wang Y, Mora P. Macroscopic elastic properties of regular lattices. Journal of the Mechanics and Physics of Solids. 2008;56(12):3459-74.

[41] Asahina D, Ito K, Houseworth J, Birkholzer J, Bolander J. Simulating the Poisson effect in lattice models of elastic continua. Computers and Geotechnics. 2015;70:60-67.

[42] Rycroft CH, Grest GS, Landry JW, Bazant MZ. Analysis of granular flow in a pebble-bed nuclear reactor. Physical review E. 2006;74(2):021306.

[43] Guo N, Zhao J. The signature of shear-induced anisotropy in granular media. Computers and Geotechnics. 2013;47:1-15.

[44] Terzaghi K, Peck RB, Mesri G. Soil mechanics in engineering practice: John Wiley & Sons, 1996.

[45] Wang S, Luna R, Onyejekwe S. Effect of Initial Consolidation Condition on Postcyclic Undrained Monotonic Shear Behavior of Mississippi River Valley Silt. Journal of Geotechnical and Geoenvironmental Engineering. 2015;142(2):04015075.

[46] Wang S, Luna R, Onyejekwe S. Postliquefaction behavior of low-plasticity silt at various degrees of reconsolidation. Soil Dynamics and Earthquake Engineering. 2015;75(259-64.

[47] Cates M, Wittmer J, Bouchaud J-P, Claudin P. Jamming, force chains, and fragile matter. Physical review letters. 1998;81(9):1841.

[48] Antony S, Kruyt NP. Role of interparticle friction and particle-scale elasticity in the shear-strength mechanism of three-dimensional granular media. Physical Review E. 2009;79(3):031308.

[49] Yamamuro JA, Abrantes AE, Lade PV. Effect of strain rate on the stress-strain behavior of sand. Journal of Geotechnical and Geoenvironmental Engineering. 2011;137(12):1169-78.

[50] Behringer RP, Bi D, Chakraborty B, Henkes S, Hartley RR. Why do granular materials stiffen with shear rate? Test of novel stress-based statistics. Physical review letters. 2008;101(26):268301.

[51] Hartley R, Behringer R. Logarithmic rate dependence of force networks in sheared granular materials. Nature. 2003;421(6926):928.

[52] A. Alshibli K, E. Roussel L. Experimental investigation of slip- stick behaviour in granular materials. International journal for numerical and analytical methods in geomechanics. 2006;30(14):1391-407.

[53] Sun Q, Jin F, Liu J, Zhang G. Understanding force chains in dense granular materials. International Journal of Modern Physics B. 2010;24(29):5743-59.

[54] Ben-David O, Rubinstein SM, Fineberg J. Slip-stick and the evolution of frictional strength.

Nature. 2010;463(7277):76.

[55] Dieterich JH, Kilgore BD. Direct observation of frictional contacts: New insights for state-dependent properties. Pure and Applied Geophysics. 1994;143(1-3):283-302.

[56] Rice JR. The localization of plastic deformation. Proceedings of the 14th International Congress of Theoretical and Applied Mechanics, 1976; 1: 207-220

[57] Asghari E, Toll D, Haeri S. Triaxial behaviour of a cemented gravely sand, Tehran alluvium. Geotechnical & Geological Engineering. 2003;21(1):1-28.

[58] Haeri SM, Hosseini SM, Toll DG, Yasrebi SS. The behaviour of an artificially cemented sandy gravel. Geotechnical & Geological Engineering. 2005;23(5):537-60.

[59] de Bono J, McDowell G, Wanatowski D. Investigating the micro mechanics of cemented sand using DEM. International Journal for Numerical and Analytical Methods in Geomechanics. 2015;39(6):655-75.

[60] Andò E, Hall SA, Viggiani G, Desrues J, Bésuelle P. Grain-scale experimental investigation of localised deformation in sand: a discrete particle tracking approach. Acta Geotechnica. 2012;7(1):1-13.

[61] Scott DR. Seismicity and stress rotation in a granular model of the brittle crust. Nature. 1996;381(6583):592.

[62] Radjai F, Jean M, Moreau J-J, Roux S. Force distributions in dense two-dimensional granular systems. Physical review letters. 1996;77(2):274.

[63] Liu C-h, Nagel SR, Schecter D, Coppersmith S, Majumdar S, Narayan O, et al. Force fluctuations in bead packs. Science. 1995;269(5223):513-5.

[64] Azéma E, Radjai F. Force chains and contact network topology in sheared packings of elongated particles. Physical review E. 2012;85(3):031303.

[65] Thornton C, Antony S. Quasi-static deformation of particulate media. Philosophical transactions-royal society of London series a mathematical physical and engineering sciences. 1998:2763-82.

[66] Yimsiri S, Soga K. DEM analysis of soil fabric effects on behaviour of sand. Géotechnique. 2010;60(6):483.

[67] Oda M. Initial fabrics and their relations to mechanical properties of granular material. Soils and foundations. 1972;12(1):17-36.

[68] Oda M. Fabric tensor for discontinuous geological materials. Soils and Foundations. 1982;22(4):96-108.

[69] Zhou W, Liu J, Ma G, Chang X. Three-dimensional DEM investigation of critical state and dilatancy behaviors of granular materials. Acta Geotechnica. 2017;12(3):527-40.

[70] Ken-Ichi K. Distribution of directional data and fabric tensors. International Journal of Engineering Science. 1984;22(2):149-64.

[71] Chang CS, Sundaram SS, Misra A. Initial moduli of particulated mass with frictional contacts. International Journal for Numerical and Analytical Methods in Geomechanics. 1989;13(6):629-44.

[72] Nicholson P, Seed R, Anwar H. Elimination of membrane compliance in undrained triaxial testing. I. Measurement and evaluation. Canadian Geotechnical Journal. 1993;30(5):727-38.

[73] Baldi G, Nova R. Membrane penetration effects in triaxial testing. Journal of Geotechnical

engineering. 1984;110(3):403-20.

[74] Martin GR, Seed HB, Finn W. Effects of system compliance on liquefaction tests. Journal of the geotechnical engineering division. 1978;104(4):463-79.

[75] Shafipour R, Soroush A. Fluid coupled-DEM modelling of undrained behavior of granular media. Computers and Geotechnics. 2008;35(5):673-85.

[76] Feng Y, Han K, Owen D. Coupled lattice Boltzmann method and discrete element modelling of particle transport in turbulent fluid flows: Computational issues. International Journal for Numerical Methods in Engineering. 2007;72(9):1111-34.

[77] Feng Y, Han K, Owen D. Combined three- dimensional lattice Boltzmann method and discrete element method for modelling fluid–particle interactions with experimental assessment. International journal for numerical methods in engineering. 2010;81(2):229-45.

[78] Wang M, Feng Y, Pande G, Zhao T. A coupled 3- dimensional bonded discrete element and lattice Boltzmann method for fluid- solid coupling in cohesive geomaterials. International Journal for Numerical and Analytical Methods in Geomechanics. 2018;42(12):1405-24.

[79] Hanley KJ, Huang X, O'Sullivan C, Kwok F. Challenges of simulating undrained tests using the constant volume method in DEM. AIP Conference Proceedings: AIP, 2013. p. 277-80.

Table

Table1 Experimental parameters

Experiment	Confining stress (kPa)	Diameter (mm)	Height (mm)	Density (g/cm^3)
Test1	50	70.8	138.1	0.57
Test2	100	70.7	138.2	0.57

Table2 Numerical parameters used in DEM simulations

Simulation properties	Specimen particles	Membrane particles
Contact model	Linear model	Linear contact bond model
Radius (m)	0.035	0.035
Density (kg/m^3)	920	2000
Friction coefficient	0.26	0
Normal stiffness (N/m)	2×10^6	541.266
Tangential stiffness (N/m)	1×10^6	180.422
Normal and tangential Bond strength (Pa)	0	1e100
Critical damp ratio	0.5	0

Table3 Thicknesses and corresponding particle-scale stiffness values for membrane

Membrane	Thickness (mm)	Normal stiffness (Pa)	Tangential stiffness(Pa)
M1	0.3	270.63	90.21
M2	0.6	541.27	180.42
M3	1	902.11	300.70

Figure

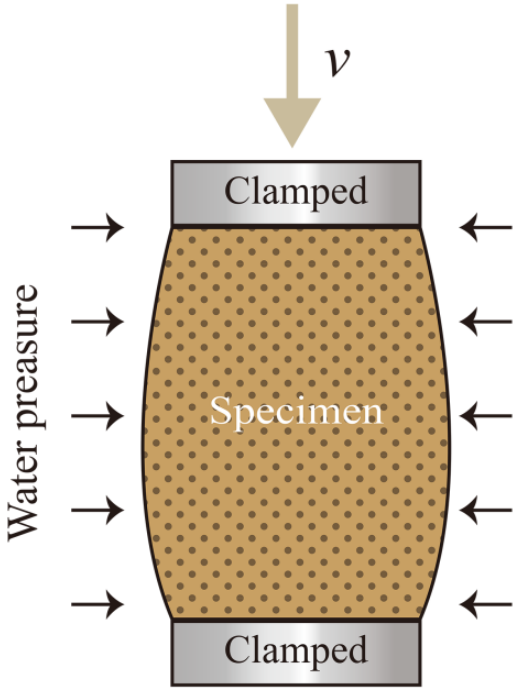

Fig. 1 Illustration of a triaxial test with a clamped membrane boundary

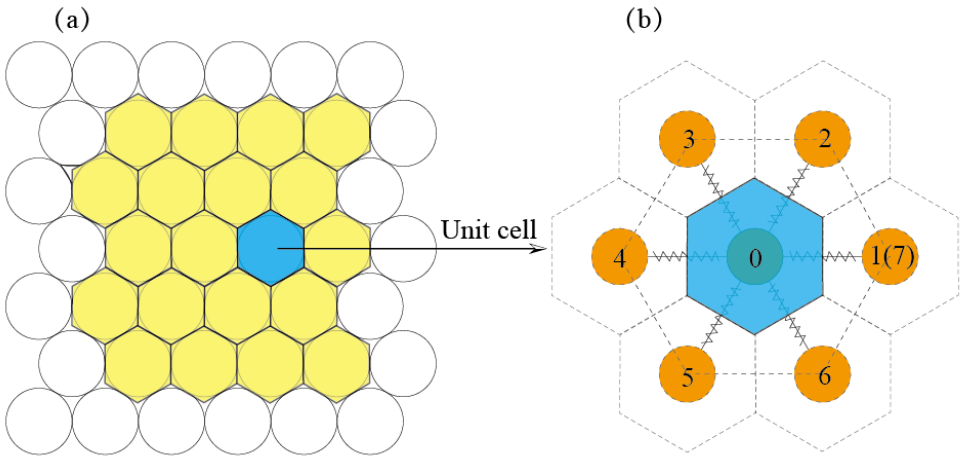

Fig. 2 Bonded particle configuration for a flexible membrane: a) hexagonal representative unit cell; b) the unit cell of a particle and its neighbouring contacts

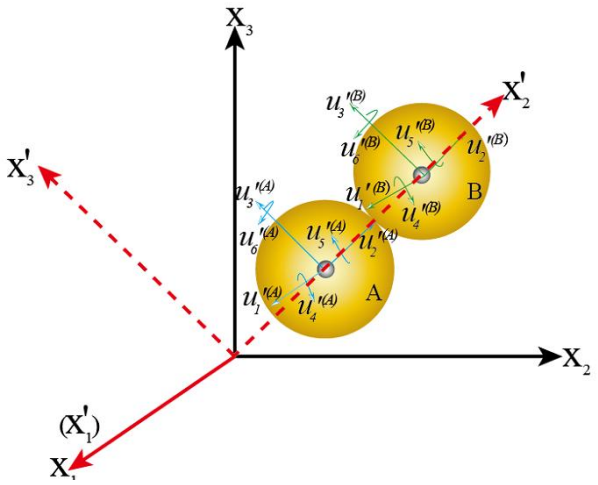

Fig. 3 Diagram for kinematics of two contacting particles in local coordinate system

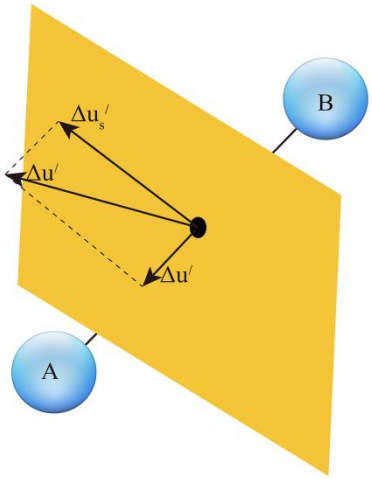

Fig. 4 Illustration for shear and normal displacement

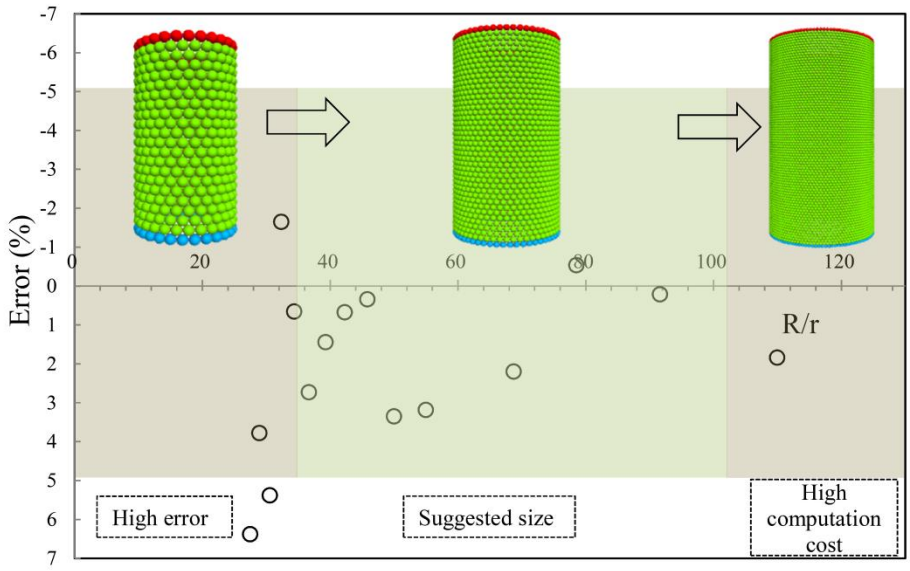

Fig. 5 Deformation errors between the analytical elastic solution and the DEM approximation

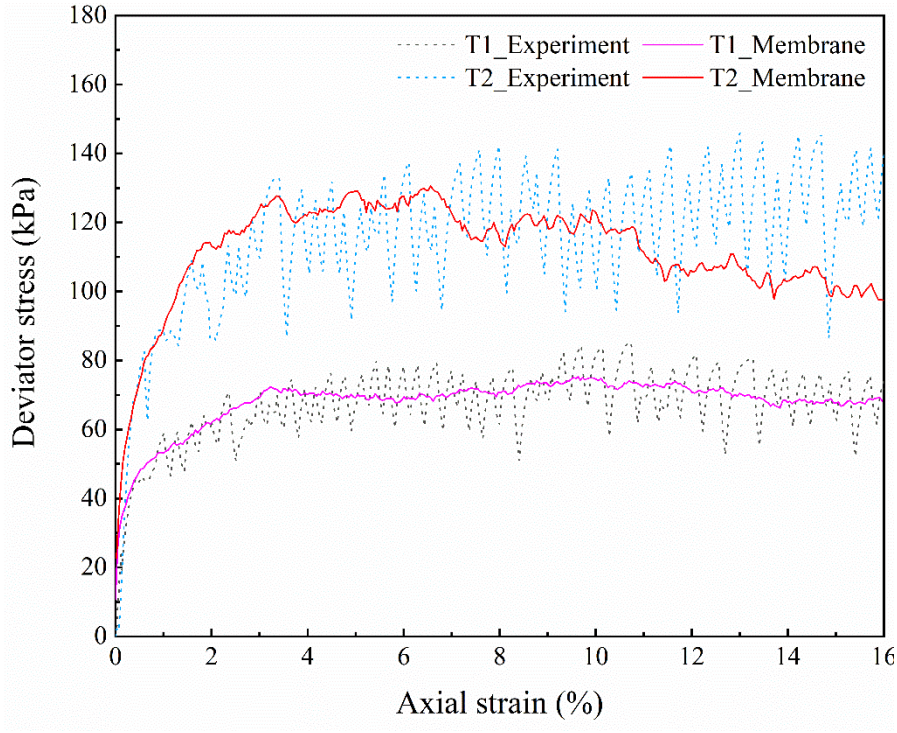

(a) Experiment and DEM modelling with membrane boundary

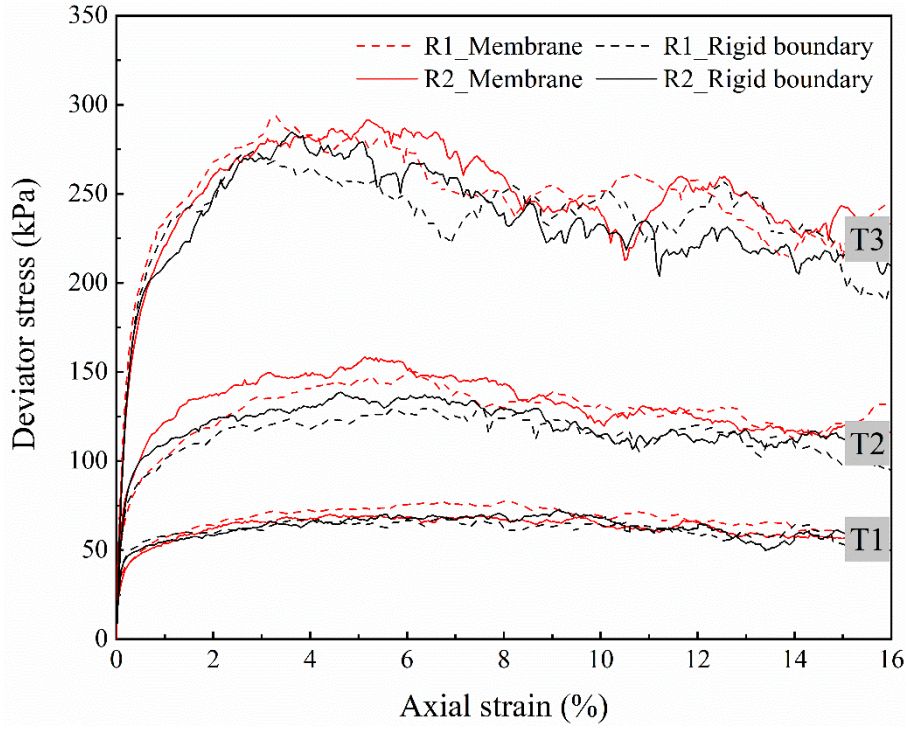

(b) Simulations with membrane and rigid boundaries

Fig. 6 Stress-strain behaviour subjected to triaxial shearing

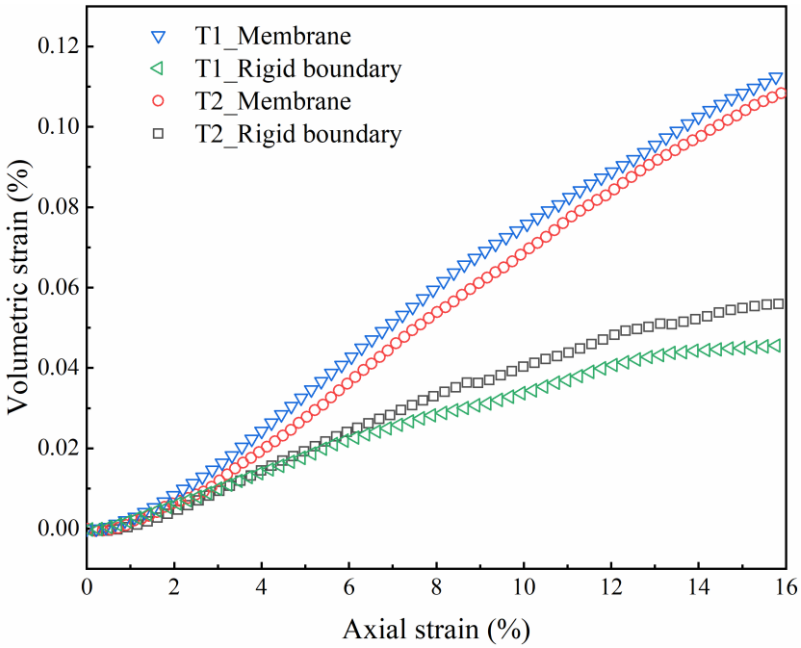

Fig. 7 Volumetric strain of triaxial testing

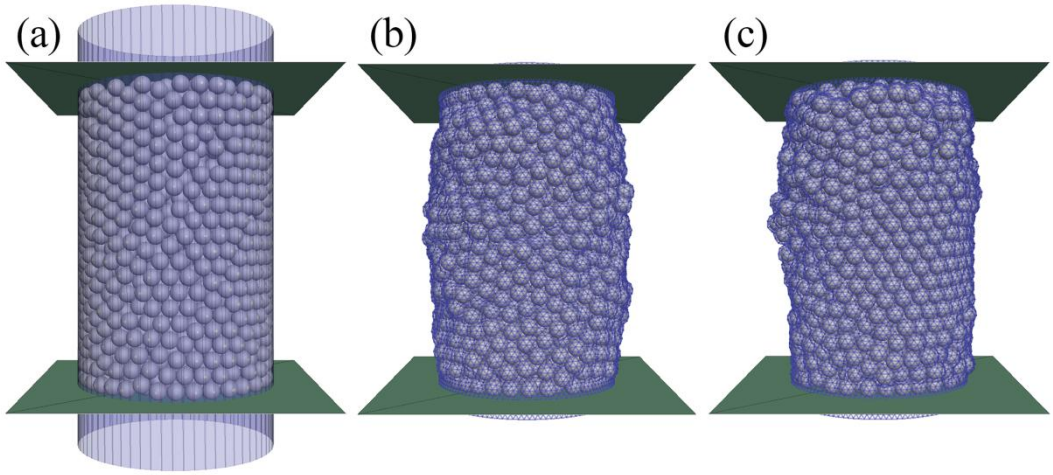

Fig. 8 The shapes of the specimen after sheard to the axial strain of 16%: (a) Rigid boundary; (b) T1_Membrane; (c) T2_Membrane

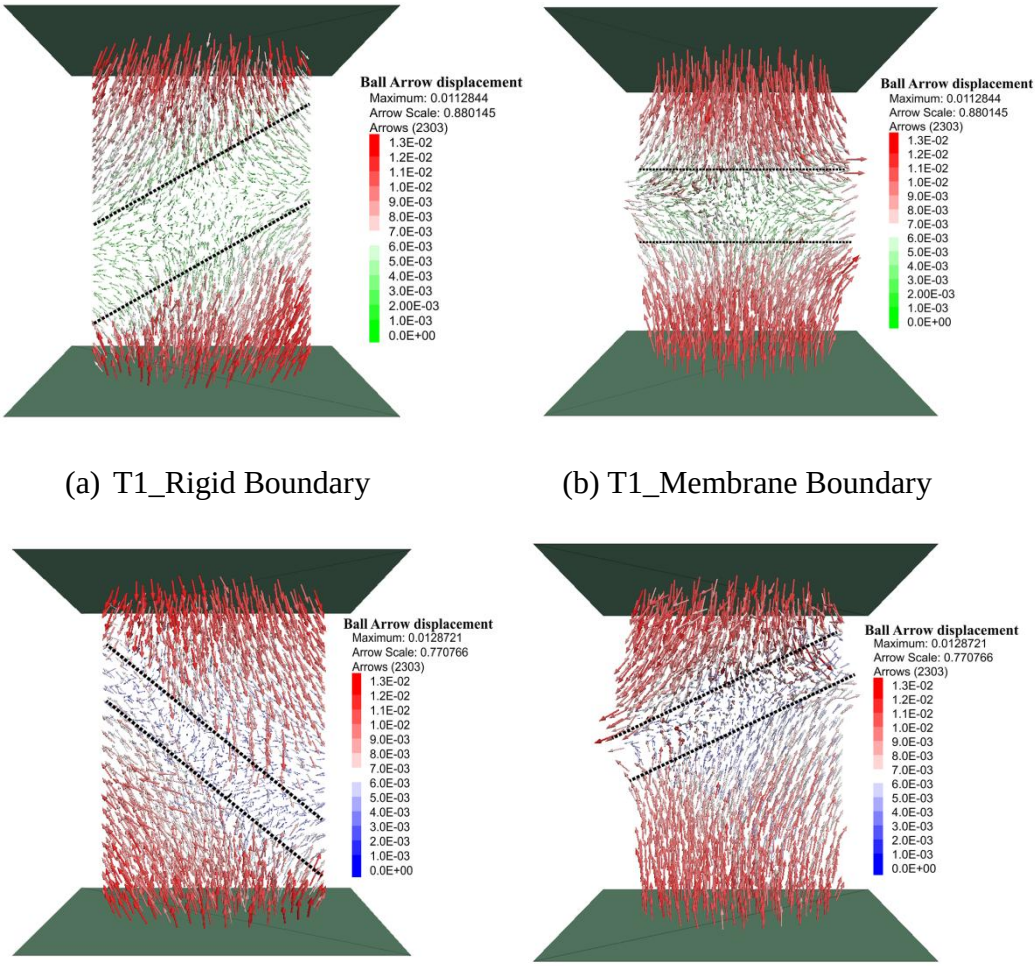

(a) T1_Rigid Boundary (b) T1_Membrane Boundary

(c) T2_Rigid Boundary (d) T2_Membrane Boundary

Fig. 9 Shear bands after triaxial shearing

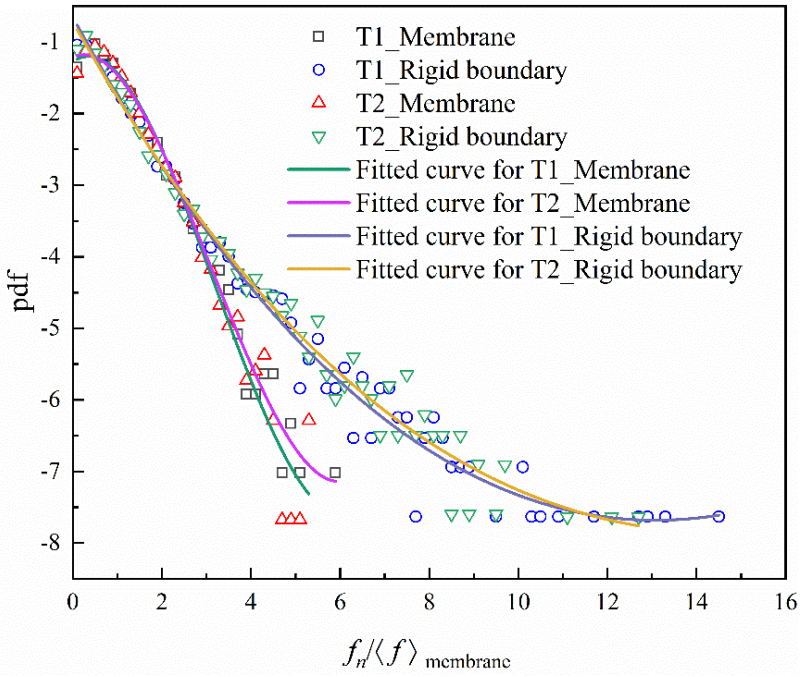

Fig. 10 Probability distribution function of normal forces $<f_n>$ normalised by the average normal force

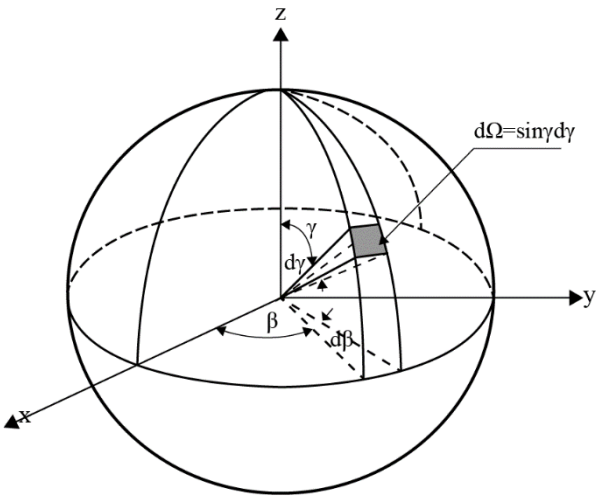

Fig. 11 Illustration of elementary solid angle

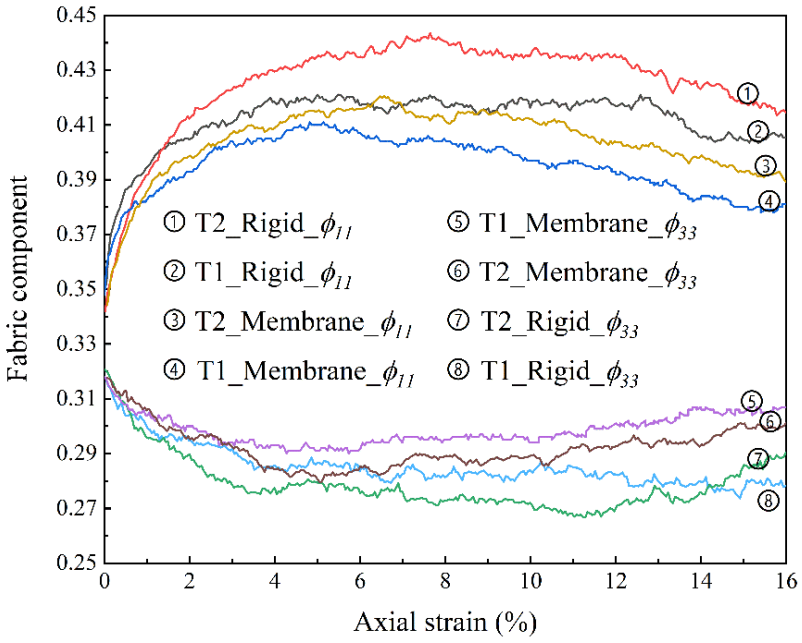

Fig. 12 Evolution of principal fabric tensors

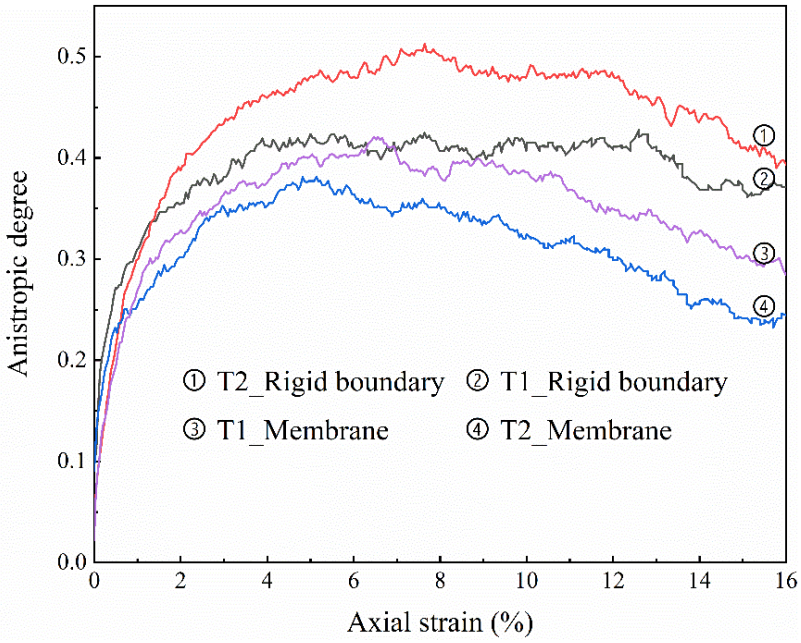

Fig. 13 Evolution of anisotropy during triaxial shearing

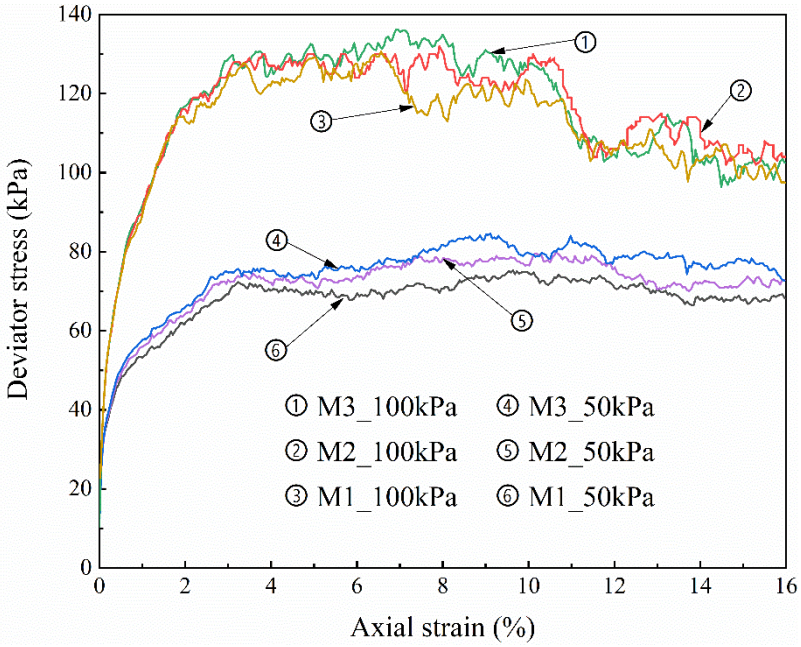

Fig. 14 Stress-strain behaviour during triaxial shearing with varied membrane thickness